Photoelectron spectrometry of atomic scandium in the region of the $3p \rightarrow 3d$ giant resonance

S. B. Whitfield* and K. Kehoe
Department of Physics and Astronomy, University of Wisconsin–Eau Claire, Eau Claire, Wisconsin 54702

R. Wehlitz
Synchrotron Radiation Center, University of Wisconsin, Stoughton, Wisconsin 53589

M. O. Krause
Department of Physics, University of Central Florida, Orlando, Florida 32816

C. D. Caldwell
National Science Foundation, 4201 Wilson Boulevard, Arlington, Virginia 22230
(Received 9 February 2001; published 20 June 2001)

A determination of the relative partial photoionization cross sections of the $3d$ and $4s$ main lines and associated satellite lines of atomic scandium in the region of the $3p \rightarrow nd,ms$ excitations has been carried out using electron spectrometry in conjunction with monochromatized synchrotron radiation. The superior resolution inherent in these measurements has revealed additional structure not previously seen in earlier experimental work, highlighting the rich and complex structure of this relatively simple open-shell atom. Relative intensities and binding energies of the $3p$ photolines are also reported. A comparison with recent many-body perturbation theory calculations in *LS* coupling shows only marginal agreement. Discrepancies between theory and experiment are thought to arise from the use of *LS* coupling and neglect of satellite channels in the calculation.

DOI: 10.1103/PhysRevA.64.022701 PACS number(s): 32.80.Fb, 32.80.Hd

I. INTRODUCTION

While experimental studies of closed-shell atoms abound, especially for the rare gases [1,2], there are still relatively few corresponding studies of open-shell atoms [3,4]. In many instances there is sometimes not more than one experiment that has been carried out on a given open-shell atom. Many of the measurements are rather old and as a result suffer from low resolution and poor statistics. This state of affairs can largely be attributed to the inherent difficulty in producing a usable atomic beam of open-shell atoms. Despite this difficulty, open-shell atoms are attractive because they generally have nonspherical charge distributions in the ground state. This leads to interesting effects in the photoionization process that cannot arise in the closed-shell case [5–7]. Furthermore, any attempt to understand atomic photoionization in a more general vein must go beyond closed-shell atoms, which make up less than 20% of the naturally occurring elements.

Atomic scandium with a lone $3d$ electron, $[\mathrm{Ar}]3d4s^2(^2D_{3/2})$, is the simplest open-shell atom to have a partially filled d subshell. This makes it especially attractive from a theoretical point of view. Nevertheless, to account for the most basic interactions involved in valence-shell photoionization entails considerable theoretical effort [8]. This is perhaps even more so in the region of the $3p \rightarrow 3d$ giant resonance. In *LS* coupling alone there are nine final ionic states and 32 channels involved in the photoionization of the $3p$, $3d$, and $4s$ subshells [9]. A comparison of recent calculations [9] with the first measurements of atomic Sc in the region of the $3p \rightarrow 3d$ giant resonance [3,10] shows marginal agreement. Part of this discrepancy is thought to be attributable to the rather low photon-energy resolution of the experiment.

With this in mind, we have undertaken a detailed experimental examination of the partial cross sections of the $3d$ and $4s$ main lines and associated satellites (ionization with excitation) in the region of the $3p \rightarrow 3d$ giant resonance. Our superior resolution, both in the monochromator and the electron spectrometer, has allowed us to make a critical comparison with theory. In addition, our results reveal a surprising degree of complexity and richness in the photoionization cross sections of the main lines and satellites, which was only hinted at in earlier measurements.

II. EXPERIMENT

The experiment was conducted in two separate runs at the University of Wisconsin Synchrotron Radiation Center (SRC). In both instances measurements were carried out on the SRC plane-grating monochromator with an undulator photon source [11]. Energy-selected photons from the monochromator are directed through a glass capillary into a resistively heated Ta crucible, where Sc atoms were produced by evaporation of the solid metal. The oven crucible simultaneously serves as the source for the photoelectrons, i.e., a slit in the crucible allows the photoelectrons to pass directly from the oven into the analyzer. This design feature allows measurements to be carried out at vapor pressures one order of magnitude less than would be required in a traditional setup in which the atoms effuse from an orifice in the cru-

*Electronic address: whitfisb@uwec.edu

cible. The oven was typically operated at around 150 W, corresponding to a temperature of about 1170 °C, producing a vapor pressure in the crucible in the lower 10^{-4} Torr range [12]. In addition, lower operating temperatures correspond to lower thermal population of excited states. According to optical data [13], the $[\mathrm{Ar}]3d4s^2(^2D_{5/2})$ excited state lies only 20 meV above the ground $^2D_{3/2}$ state. At these temperatures, thermal excitation leads to 56% of the target atoms in the $^2D_{5/2}$ excited state and only 44% in the ground state. The electrons were energy analyzed in a spherical sector-plate analyzer with a nominal resolution of 1% of the pass energy. To preclude the influence of the angular distributions on the measured intensities, the analyzer was set to the magic angle $\theta_m = \frac{1}{2}\cos^{-1}(-1/3p)$. In a set of separate calibrations using Ne $2s$ photoelectrons, the polarization p of the ionizing radiation was found to be 99(1)%, corresponding to $\theta_m = 54.8°$.

Photoelectron spectra were collected in two different modes: the photoelectron-spectrometry (PES) mode, in which the electron intensity is recorded as a function of the electron kinetic energy at a fixed photon energy, and the constant-ionic-state (CIS) mode in which spectra are recorded by simultaneously scanning the incident photon energy and the accelerating (retarding) voltage of the source cell so as to always observe electrons that correspond to the same final ionic state.

The resolution of a CIS spectrum depends solely on the bandpass of the monochromator. The resolution of the electron spectrometer only plays a role insofar as it must be capable of isolating single final states of the ion. In the case of both runs, wide open slits, $255\times150\,\mu$m [(entrance)×(exit)], where more than adequate to provide a resolving power sufficient to resolve even the narrowest features. The bandpass of the monochromator for these slit settings was found to be 20(3) meV at 47.692 eV, as determined from a convoluted fit of the Ne $2s\rightarrow5p$ autoionization resonance. The position of this resonance, 47.692 eV [14], as well as the Ar $3s\rightarrow6p$ autoionization resonance, 28.511 eV [15], also served to calibrate the photon energy.

Because of the broad photon energy regions measured, 29.0–40.4 eV or 34.0–40.4 eV in 10-meV steps, five or three separate CIS scans were recorded covering the aforementioned photon-energy ranges and then ''stitched'' together. In each case adjacent spectra at lower photon energies overlapped those at higher photon energies by ten points. In all cases no data were obtained in the region between approximately 32.5 and 33.5 eV. This was done to save time in the data acquisition process and because minimal structure exists in this region. Changes in the photon flux during the course of the CIS scan were monitored by simultaneously recording the current output of a 90% transmission Ni mesh just downstream of the exit mirror of the monochromator. A detailed explanation of how this and other calibrations were employed to correct the CIS spectra for changes in the oven yield and the influence of the background are given in Sec. II of Ref. [16]. Following the application of these procedures, each CIS spectrum corresponds to the relative partial cross section of the feature in question. To assure that the stitching

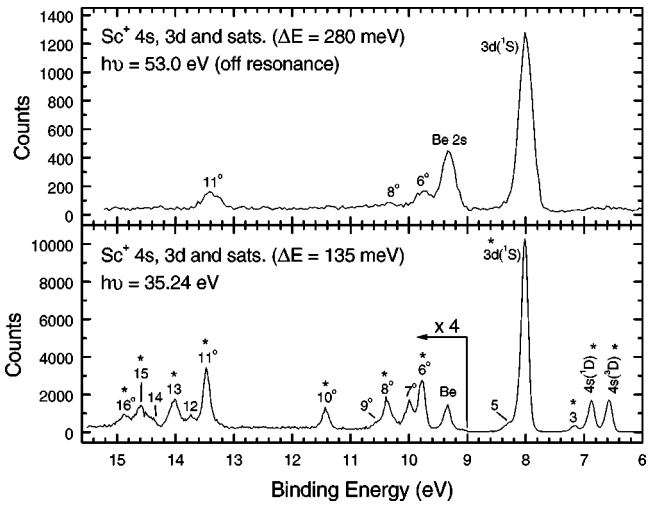

FIG. 1. High-resolution PES spectrum of the $3d$, $4s$ main and satellite lines recorded at the magic angle at the maximum of the $3p\rightarrow3d$ giant resonance, lower panel. The step size is 20 meV. Off-resonance PES spectrum recorded above the region of the $3p$ excitations, upper panel. The step size is 40 meV. See text for additional details.

procedure yielded correct relative partial cross sections, one CIS spectrum of the $3d(^1S)$ main line was recorded over the whole range from 29.0 to 40.4 eV in 30-meV steps. Comparison of this spectrum with its composite counterpart gave nearly identical results, apart from the difference in resolution due to the different step sizes. This spectrum was also necessary to normalize the composite spectrum in the lower photon-energy region (29.0–32.5 eV) with that in the higher photon-energy region (33.5–40.4 eV). The composite $3d(^1S)$ spectrum then provided the means by which all other CIS spectra were normalized with respect to each other as outlined below. CIS spectra took from 30 to 90 min to record, depending on the strength of the feature and the initial beam current in the storage ring.

For the PES spectra, no correction due to transmission effects was deemed necessary. Based on previous calibrations and the typical response of the analyzer, at no time was the retardation of the photoelectrons sufficiently large as to merit transmission corrections. Furthermore, spectra recorded at the same photon energy but different pass energies showed nearly identical intensity ratios among the various peaks in the spectrum, giving further indication that transmission effects, if present, are negligible.

Normalization between the various composite CIS scans was accomplished as follows. The integrated intensity of the $3d(^1S)$ main line, corresponding to the $[\mathrm{Ar}]4s^2(^1S)$ ionic configuration at $h\nu = 35.24$ eV, Fig. 1, was arbitrarily set to 100. Similarly, the maximum value of this line as recorded in the CIS spectrum of Fig. 2 at $h\nu = 35.24$ eV was also set to 100. The remaining CIS spectra of the $4s$ main lines and satellites in the upper photon-energy region (about 33–40.4 eV) were then normalized so that their relative intensities at 35.24 eV were equal to the relative intensities derived from the PES results recorded at $h\nu = 35.24$ eV. The results are summarized in Table I. To normalize the CIS spectra of the $4s$ main lines and satellites in the lower photon-energy re-

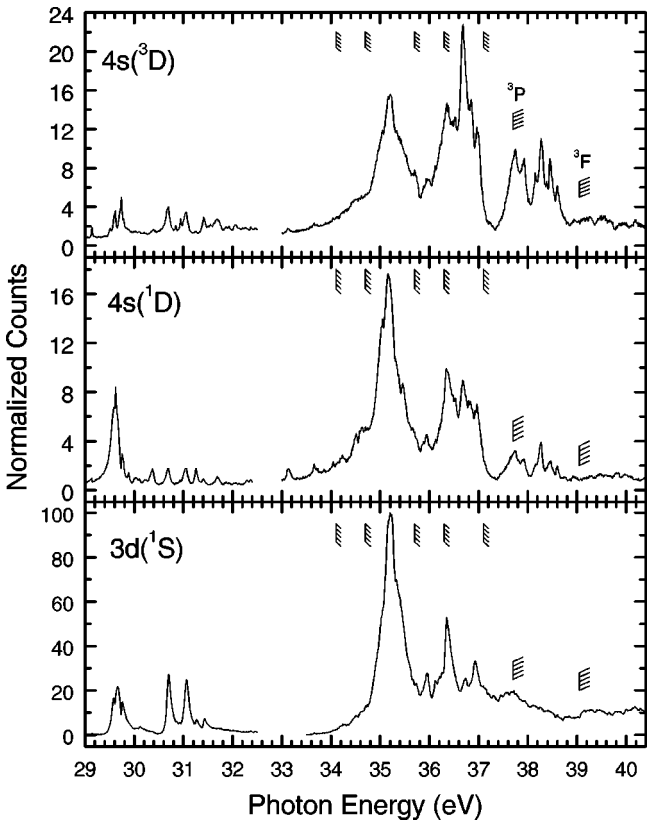

FIG. 2. CIS scans of the main lines recorded at the magic angle in the region of the $3p \rightarrow nl$ resonances. The monochromator bandpass is better than 20 meV and the step size is 10 meV. Spectra are normalized so that their relative intensities can be directly compared. Several of the $3p$ ionization thresholds are shown. Those labeled correspond to the $3p^5 3d 4s^2$ configuration, and the others to the $3p^5 3d^2 4s$ configuration. See text for additional details.

gion (29.0 to about 32.5 eV) with respect to each other, and those in the higher photon-energy region, a PES spectrum was recorded on the resonance at $h\nu = 31.06$ eV (see Fig. 2). The integrated intensity of the $3d(^1S)$ main line in the PES spectrum at this photon energy was then set equal to 24.9—the value of the $3d(^1S)$ main line in the CIS spectrum of Fig. 2 at this energy. The ratios of the $4s$ and satellite lines to the main $3d(^1S)$ line derived from this PES spectrum were then used to normalize the remaining CIS spectra at $h\nu = 31.06$ eV.

III. RESULTS AND DISCUSSION

A. PES results

Two photoelectron spectra of atomic scandium are shown in Fig. 1. The high-resolution spectrum in the lower panel was recorded at $h\nu = 35.24$ eV, the maximum of the $3p \rightarrow 3d$ giant resonance. For the sake of brevity, we will refer to the main lines according to the subshell of the electron which is removed in the photoionization process, and *not* by the ionic state that is left behind. That is, the $3d(^1S)$ designation refers to the $[\mathrm{Ar}]4s^2(^1S)$ final-ionic state, and $4s(^{3,1}D)$ to the $[\mathrm{Ar}]3d4s(^{3,1}D)$ final-ionic states. The binding energy scale was established by setting the $3d(^1S)$ photoline to 8.015 eV as derived from optical data [13]. Clearly visible are the main photoelectron lines originating from the $3d$ and $4s$ subshells as well as numerous satellite lines. Their binding energies, relative intensities with respect to the $3d(^1S)$ peak, and assignments based on a comparison with optical data [13] are given in Table I. A comparison to the binding energies reported by Wetzel [10] is also given. Features with a superscript 'o' indicate satellites with odd parity, and those with an asterisk above them indicate features for which a CIS scan was recorded. The peak marked as Be $2s$ is a result of contamination of the oven with Be from a previous experiment in which the same crucible was used. Compared to the earlier data of Refs. [3,10], the two $4s$ main lines are now completely resolved, as are many of the satellites. The superior resolution in this work has allowed us to catalog more than twice as many satellites as seen previously in this binding-energy region. In addition, we are also able to specify the specific term of the satellite with greater certainty than previously. Overall, there is quite good agreement between our results and those of Ref. [13]. It is worth noting that of all the observed intensity at this resonance photon energy, about 28% is in the satellite channels.

The upper spectrum was recorded off resonance at a photon energy of 53.0 eV, above all $3p$ thresholds. Due to the very low cross section off resonance, a larger pass energy was required in order to obtain a reasonable count rate. With regard to the main lines, only the $3d(^1S)$ is visible, with the $4s$ main lines virtually nonexistent. This is consistent with an off-resonance PES measurement taken with He $I\alpha$ radiation [17], where the $3d(^1S)$ main line is more than 33 times as intense as either $4s$ line. Clearly evident are the correlation satellites 6, 8, and 11. According to Table I, feature 6 could be composed of two satellites with different configurations, $[\mathrm{Ar}]3d^2(^1S)$ and $[\mathrm{Ar}]3d4p(^1D^o)$. There is no ambiguity in the assignment of satellites 8 and 11, where their ionic-state configurations are $[\mathrm{Ar}]3d4p(^1P^o)$ and $[\mathrm{Ar}]4s4p(^1P^o)$, respectively. From a least-squares fit of the data we find the following intensity ratios at $h\nu = 53.0$ eV: $I(\text{sat. 6}):I(3d(^1S)) = 0.122(6)$, $I(\text{sat. 8}):I(3d(^1S)) = 0.045(5)$, and $I(\text{sat. 11}):I(3d(^1S)) = 0.110(5)$.

The origin of these satellites is most simply attributed to initial-state configuration interaction (ISCI). For simplicity, we restrict our discussion to LS coupling, then the configurations $[\mathrm{Ar}]3d^2(^1D)4s(^2S)\ ^2D$, $[\mathrm{Ar}]3d(^2D)4p^2(^1S)\ ^2D$, and $[\mathrm{Ar}]4s(^2S)4p^2(^1D)\ ^2D$ mix with the primary $[\mathrm{Ar}]3d4s^2\ ^2D$ configuration. That is, the ground-state wave function is of the form

$$|\psi_g\rangle = \alpha|[\mathrm{Ar}]3d4s^2\ ^2D\rangle + \beta|[\mathrm{Ar}]3d^2(^1D)4s(^2S)^2D\rangle + \gamma|[\mathrm{Ar}]3d(^2D)4p^2(^1S)^2D\rangle + \delta|[\mathrm{Ar}]4s(^2S)4p^2(^1D)^2D\rangle, \quad (3.1)$$

where α, β, γ, and δ are mixing coefficients. We note that the odd satellites cannot arise from final-ionic-state configuration interaction (FISCI) as their parity is different from the ionic states associated with the $3d$ and $4s$ main lines. This is not true for the even parity configuration of satellite 6,

TABLE I. Binding energies of the scandium main lines and satellites and their relative intensities measured at 55° and $h\nu = 35.24(4)$ eV.

Line	Binding energy (eV)			Rel. int. (%)	Assignment[a]
	This work	Ref. [10]	Ref. [13][b]		Ref. [13]
1	6.58(2)	6.56	6.573(22)[c]	15.6(5)	$3d4s(^3D)$
2	6.87(2)	6.86	6.875	15.6(5)	$3d4s(^1D)$
3	7.16(2)		7.168(23)	3.4(5)	$3d^2(^3F)$
4	8.015[d]	8.01	8.015	100.0	$4s^2(^1S)$
5	8.28(2)		8.328	5.6(5)	$3d^2(^1G)$
6	9.78(2)	9.82	9.778 9.794	6.7(5)	$3d^2(^1S)$ $3d4p(^1D^o)$
7	10.00(2)		9.990(52)	5.6(5)	$3d4p(^3F^o)$
8	10.36(2)	10.31	10.381	4.3(5)	$3d4p(^1P^o)$
9	10.55(2)		10.571	1.1(5)	$3d4p(^1F^o)$
10	11.42(2)	11.47	11.424(42)	2.7(5)	$4s4p(^3P^o)$
11	13.46(2)	13.51	13.468	8.0(5)	$4s4p(^1P^o)$
12	13.73(2)		13.710(24)	1.8(5)	$3d5s(^3D)$
13	14.02(2)	14.09	13.996(16)	4.4(5)	$3d4d(^3D)$
14	14.41(2)		14.428(19)	1.5(5)	$3d4d(^3F)$
15	14.61(2)	14.64	14.579(10)	3.1(5)	$3d4d(^3P)$
16	14.87(2)		14.818(32) 14.894	2.0(5)	$3d5p(^3F^o)$ $3d4d(^1S)$

[a]All assignments implicitly include an argon core.

[b]All energies correspond to the weighted average of the various J components of the final term.

[c]The uncertainty, when stated, corresponds to the maximum spread of the fine-structure components.

[d]Reference energies by which the binding-energy scale was determined.

$3d^2(^1S)$, which could also arise from FISCI by mixing with the $4s^2(^1S)$ final-ionic-state configuration associated with photoionization of the $3d$ line.

All of these satellites can also arise from continuum-state configuration interaction (CSCI) [18]. For example, satellite 8 would result from the following transition:

$$[\mathrm{Ar}]3d4s^2(^2D)+h\nu \rightarrow [\mathrm{Ar}]3d4p(^1P^o)\varepsilon s,d,g(^2P,\ ^2D,\ ^2F). \tag{3.2}$$

The photoionization amplitude in this picture will involve overlap matrix elements of the type $\langle 4s|\varepsilon s,d,g\rangle$. These satellites in this picture are usually largest at threshold and diminish as their kinetic energies increase because of the rapid variations of the radial part of the continuum wave function. As we did not record an off-resonance PES spectrum near the ionization threshold of these satellites, we cannot comment on how their intensities vary with photon energy. While satellite 8 appears to be quite weak at $h\nu = 53$ eV, the same cannot be said for satellite 11.

However, because of the photon energy at which this spectrum was recorded, it seems unlikely that the origin of these satellites is primarily due to CSCI. This is because this photon energy is substantially greater than the excitation energy of each satellite (the difference between the binding energy of the satellite and its corresponding main line.) The ratio of the photon energy to the excitation energy is about 30, 23, and 10 for sats 6, 8, and 11, respectively. Typically, CSCI satellites effectively vanish when this ratio reaches about 3 [18].

On resonance both the even and odd parity ionic-states are populated via autoionization. With the previous picture of ISCI in mind, we can understand the origin of the main lines and all the satellites as follows. For simplicity, consider only $3p \rightarrow 3d,4s$ excitation of the ground state listed above, Eq. (3.1), which leads to the following excited state:

$$\begin{aligned}|\psi^*\rangle = {} & \alpha'|[\mathrm{Ne}]3s^2 3p^5 3d^2 4s^2(^2P,\ ^2D,\ ^2F)\rangle \\ & + \beta'|[\mathrm{Ne}]3s^2 3p^5 3d^3 4s(^2P,\ ^2D,\ ^2F)\rangle \\ & + \gamma'|[\mathrm{Ne}]3s^2 3p^5 3d^2 4p^2(^2P,\ ^2D,\ ^2F)\rangle \\ & + \delta'|[\mathrm{Ne}]3s^2 3p^5 4s^2 4p^2(^2P,\ ^2D,\ ^2F)\rangle. \end{aligned} \tag{3.3}$$

Production of the main lines is most likely to be due to the decay of the $3s^2 3p^5 3d^2 4s^2$ part of the excited state, where the $3d(^1S)$ line arises when both $3d$ electrons are involved in the decay and the $4s(^{1,3}D)$ lines arise when one $4s$ and one $3d$ electron are involved in the decay. If during this latter decay the remaining $4s$ electron is shaken up, then satellites of the type $3d5s$ are created, e.g., sat. 12. The $4s$ main lines can also arise from the decay of the $3s^2 3p^5 3d^3 4s$ contribution when two $3d$ electrons take part in the decay. The $3d(^1S)$ line can also arise from the decay of the

$3s^2 3p^5 4s^2 4p^2$ part of the excited state when both $4p$ electrons participate in the decay. When one $4s$ and one $4p$ electron are involved in the decay, then satellites of the type $4s4p$ are produced, e.g., sats. 10 and 11. The appearance of these satellites at this excitation energy is strong evidence that this resonance cannot be due to $3p \rightarrow 3d$ excitation alone and must include $3p \rightarrow 4s$ transitions. Otherwise, these odd-parity satellites cannot be produced with the strength they are observed to have. The even satellites of the type $3d^2$, e.g., sats. 3 and 5, can arise from decay of the $3s^2 3p^5 3d^3 4s$ excited state when one $3d$ and the $4s$ electron participate in the decay, or from decay of the $3s^2 3p^5 3d^2 4s^2$ and $3s^2 3p^5 3d^2 4p^2$ excited states, where the $3d$ electrons *do not* participate in the decay. If one of the $3d$ electrons is shaken up during this decay, then satellites of the type $3d4d$ are produced, e.g., sats. 13–15. Finally, the odd satellites of the type $3d4p$, lines 6–9, can arise from the decay of the $3s^2 3p^5 3d^2 4p^2$ part of the excited state when one $3d$ and one $4p$ electron participate in the decay. In all of these transitions, the correct parity of the final state will be assured by the orbital angular momentum of the continuum electron.

A PES spectrum of the $3p$ photopeaks of atomic scandium is displayed in Fig. 3. This spectrum is practically identical to one reported recently [19]. The binding-energy scale was determined in a similar spectrum in which a small amount of Ne was leaked into the oven. The difference in kinetic energies of the $3p(^3F)$ line and the Ne$2s$ line then served to establish the binding energy of the $3p(^3F)$ line. The binding energies of the other terms were determined from a least-squares fit of this spectrum, using Pearson-7 functions, and one recorded with a lower pass energy, inset of Fig. 3, so that the $3p(^1F)$ and the $3p(^1D)$ terms could be better resolved. While the fit is highly suggestive of the presence of two partially separated lines in the binding-energy range between 41 and 42 eV, the statistics are not good enough to be definitive with regard to their binding energies. Assignments of the peaks are taken from the Hartree-Fock calculations of Ref. [19]. The vertical bars in the figure correspond to the calculated binding energies of Ref. [9] using a multiconfiguration Hartree-Fock (MCHF) approach. In Ref. [9] the ordering of the ^1F, ^1D, and ^3D terms is different from those of Ref. [19]. Reference [9] predicts the ordering of these terms from highest to lowest binding energy to be ^3D, ^1F, and ^1D, respectively. The ordering given in Ref. [19] would appear to be a more reasonable choice, as one would expect from statistics alone that the ^3D term would be more intense than the ^1D term. Furthermore, the triplet term would normally have a lower binding energy than a singlet term with the same value of L. Nevertheless, the MCHF calculations of Ref. [9] predict an inversion of these terms.

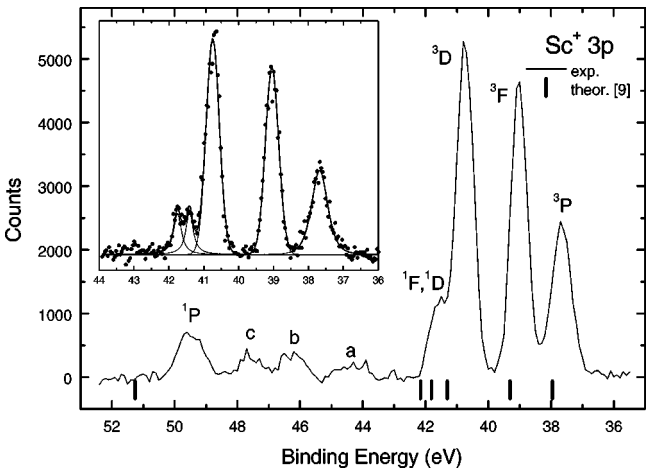

FIG. 3. PES spectrum of the $3p$ main lines and satellites recorded at the magic angle at $h\nu = 90$ eV. The inset is a higher-resolution spectrum recorded over a smaller binding-energy range. It includes a least-squares fit of the data and its decomposition.

In addition to the main $3p$ lines, several satellites are also evident, indicated by roman letters. Table II summarizes the experimental binding energies and intensities at $h\nu = 90$ eV of these features including a comparison with theory and the experimental results of Refs. [19,20] recorded at $h\nu$

TABLE II. Binding energies of the scandium $3p$ lines and satellites and their relative intensities measured at 55° and $h\nu = 90.00(4)$ eV.

	Binding energy (eV)				Rel. int. (%)	
Line	This work	Theory [9]	ΔE	Ref. [19]	This work	Ref. [20]
$3p(^3P)$	37.70(3)	37.96	−0.26	37.5(2)	65(3)	70(10)
$3p(^3F)$	39.05(3)[a]	39.31	−0.26	38.9(2)	100	100
$3p(^3D)$	40.76(3)	41.31[b]	−0.55	40.6(2)	116(6)	110(10)
$3p(^1D)$	41.42(3)	41.81[c]	−0.39	41.4(2)	14(4)	30(10)
$3p(^1F)$	41.77(3)	42.16[d]	−0.39	41.4(2)	15(4)	
a	44.4(1)				6(2)	
b	46.30(8)			45.3–46.8	11(3)	10(10)
c	47.66(8)			46.8–48.1	10(3)	10(10)
$3p(^1P)$	49.52(3)	51.26	−1.74	48.1–50.2	23(2)	20(10)

[a]Reference energy by which the binding-energy scale was determined.
[b]Reference [9] assigns this peak as a ^1D term.
[c]Reference [9] assigns this peak as a ^1F term.
[d]Reference [9] assigns this peak as a ^3D term.

$=120$ eV. Comparing our results with the recent experiment of Refs. [19,20] shows generally good agreement for both the binding energies and relative intensities. We note, however, that the binding energies of Ref. [19] are systematically lower than ours, although still within the error of each measurement. Furthermore, the negligible variation in the relative intensities between the two measurements, which were recorded 30 eV apart in photon energy, indicates little change in the relative photoionization dynamics of the various $3p$ terms over this energy range.

Interestingly, there appears to be a significant difference in the width and shape amongst the $3p$ terms. According to the fit of the higher-resolution spectrum, the full-width half maximum (FWHM) of the Lorentzian-shaped $3p(^3P)$ term is about 0.54 eV, which is statistically larger than either the $3p(^3F)$ or the $3p(^3D)$ terms, which have widths of about 0.45 eV. The widths of the remaining components, the $3p(^1F)$ and $3p(^1D)$, are nearly the same, about 0.26 eV. For the pass energy used to record this spectrum, the resolution of the analyzers is at best about 0.20 eV, although this was not rigorously determined. One possible explanation for the observed differences in shape and FWHM is that the fine-structure components of the $3p(^3P)$ are spread more than for the other terms, thereby leading to a larger observed width. Clearly calculations on the fine-structure level as well as improved experimental resolution will be required to fully explain these observations.

Calculated binding energies are in satisfactory agreement with experiment for all terms except the $3p(^1P)$, which is substantially off, 1.74 eV. In all cases, the calculated binding energies overestimate the experimental binding energies. However, energy splittings from one term to the next are in reasonably good agreement with experiment, except for the $3p(^1P)$. At this photon energy, there are no calculations of the cross sections of these terms so it is not possible to compare the relative intensities with theory.

B. CIS results

1. Main lines

The dynamical behavior of the energy dependence of the partial cross section as a function of photon energy is revealed in greatest detail by a CIS spectrum. Conversely, a CIS spectrum of a known line corresponding to a particular ionic state also helps to identify excited states of the neutral atom and yield their decay probabilities into the various exit channels. Figure 2 shows the CIS spectra of the $3d$ and $4s$ main lines ($[\mathrm{Ar}]4s^2(^1S)$ and $[\mathrm{Ar}]3d4s(^{3,1}D)$ ionic states, respectively) covering the photon energy region from 29.0 to 40.4 eV. This includes the region of the $3p\rightarrow 3d$ excitations, which in *LS* coupling alone corresponds to nine different transitions from the single $[\mathrm{Ne}]3s^23p^63d4s^2(^2D)$ ground-state configuration. Also included are the $3p\rightarrow nd$, $ms(n>3,m>4)$ excitations converging to the $[\mathrm{Ne}]3s^23p^53d4s^2(^3P,^3F)$ limits in the single-configuration case as well as those transitions converging to the higher-lying limits (^3D, ^1D, ^1F, ^1P) whose members appear below excitation energies of 40.4 eV [if the ground state of Eq. (3.1) is considered, then there can also be $m=4$ transitions, see Eq. (3.3)]. The positions of the ^3P and ^3F thresholds as given in Table II are also indicated. Also shown are five of the ionization thresholds associated with $3p$ ionization of the secondary configuration $[\mathrm{Ne}]3s^23p^63d^24s(^2D)$ of the ISCI ground state, see Eq. (3.1). These thresholds are briefly discussed in Ref. [3], and in more detail in Ref. [10], where their energies are given as 34.1(4), 34.7(4), 35.7(4), 36.3(4), and 37.1(4) eV. These thresholds were determined from measurements of the kinetic energies of a group of Auger lines and their final-state energies obtained from optical data [13]. This particular Auger group arises from $[\mathrm{Ne}]3s^23p^53d^24s\rightarrow[\mathrm{Ne}]3s^23p^63d\varepsilon_{\ell}$ decay, where they appear at photon energies above 34.1 eV, the lowest-lying $[\mathrm{Ne}]3s^23p^53d^24s$ threshold, and at kinetic energies below 18.0 eV [10]. While these five thresholds could be determined from the Auger data, we note that in *LS* coupling alone there are *32 possible thresholds*. The presence of these low-lying ionization thresholds will be crucial for understanding the appearance of the main line and satellite partial cross sections discussed below. The spectra are displayed without any correction to the photon-energy scale. According to our calibrations, see Sec. II, a photon energy of 47.731 eV should be shifted down by 0.038 eV, while a photon energy of 28.523 eV should be shifted down by 0.012 eV. This roughly corresponds to a constant offset in wavelength of $+0.25(3)$ Å.

These spectra, and all other CIS spectra, can be reasonably divided into two regimes, a lower photon-energy region (region I) covering the range from 29 to about 32.5 eV, and a higher region (region II) covering about 33.0–40.4 eV. The weakest and narrowest features all occur in region I. In addition, most features in this region are better resolved, i.e., there is generally less overlap than for those in region II. In contrast to earlier CIS measurements, where a fully resolved $3d$ line and a sum of the two $4s$ lines was reported [3,10], the two $4s$ lines are now completely resolved, as are numerous satellite lines, revealing significantly more structure in all cases. The latter observation is directly attributable to the improved resolution with very good statistics in this measurement. In the earlier measurements a resolving power of about 300 was obtained, while in our case it is nearly 2400. Nevertheless, apart from resolution and superior statistics, the two experiments reproduce each other very nicely. Not only are the same main features seen in each case, but the relative intensities amongst the various features are also well reproduced, including the overall weaker intensity of the features in region I as compared to region II.

One of the most striking aspects of these spectra is the sheer complexity they reveal. In region II it is clear that all the very broad peaks, e.g., that at 35.24 eV that appears in all spectra, cannot be attributed to one or even two resonances but likely result from numerous resonances that not only overlap, but probably also interact. This is in contrast to the other $3d$ transition metals, particularly Mn [3,16], Fe [3,21,22], Co [3], and Ni [3,22], where the positions of the dominant $3p\rightarrow 3d$ transitions are rather unambiguous. For these transition-metal atoms, these resonances are usually, slightly asymmetric Fano profiles that dominate the entire spectrum. According to Refs. [3,10], the peak centered at

35.24 eV is composed of two resonances with energies of 35.2(1) and 35.3(1) eV. They were tentatively assigned as arising from the $3p^5 3d^2(^1G,\ ^3F)4s^2(^2F)$ excited-state configuration. This assignment is disputed in Ref. [9] where this peak is assigned to the $3p^5 3d 4s^2(^3P)5s(^2P)$ excited state. A detailed comparison of theory with our results as discussed in Sec. III C makes this assignment seem unlikely. Because of the complexity of these spectra in region II, no attempt has been made to determine resonance positions. Attempting to fit this region with multiple Fano or Shore profiles would not only be difficult and extremely tedious, but essentially pointless, as such simple parametrizations do not account for the interaction of closely spaced resonances. Simply marking peak positions is only marginally helpful, as many of these lines are somewhat asymmetric and, hence, the resonance position will not coincide with the peak maximum. Additionally, what appears to be two adjacent peaks could in fact be one peak with a window. Clearly, a Herculean effort will be required to merely classify the various resonances and their positions, let alone explain their intensity distributions, particularly for region II.

Nevertheless, we can make some additional qualitative remarks regarding the structure of region II. The appearance of a large number of overlapping resonances is very likely due to the large number of $3p \rightarrow nd$, ms excitations that can take place from the ISCI ground state, Eq. (3.1). Because many of these transitions take place at photon energies above the lowest experimentally observed $[\mathrm{Ne}]3s^2 3p^5 3d^2 4s$ ionization threshold at $h\nu = 34.1$ eV, the intermediate excited states can autoionize into Sc II channels associated with these thresholds. These additional decay pathways will subsequently lead to broader lines in region II than in region I where such autoionization is not possible. This is precisely what is observed: the narrowest resonance features all occur in region I.

Unlike region II, the majority of the resonances that appear in region I are relatively well isolated and for the most part rather symmetric in shape. This makes it much easier to ascertain resonance positions than in region II. Figure 4 shows a comparison of the main lines with each other in region I. The ordinate of each main line has been arbitrarily scaled to facilitate the comparison. Numerical designations are given for all features that unambiguously appear in each main line channel. For those features that are less definitive, roman letters are used. The resonance energies were determined by simply noting the peak positions of the resonances, and in some cases windows. Hence, the reported energies that are summarized in Table III, should only serve as a guide to the exact resonance energy. The photon energies stated in Table III have been corrected by applying a linear interpolation to the nominal photon energies (those displayed in Fig. 4). This correction is derived from the photon-energy calibrations discussed in Sec. II B 1 above. The results obtained in Ref. [10] are also given.

The peculiar appearance of the resonances clustered around 29.65 eV deserves some additional discussion. In the $3d(^1S)$ channel it appears that there is a single broad, slightly asymmetric resonance, feature 2, which has two bites taken out of it. These correspond to the windows

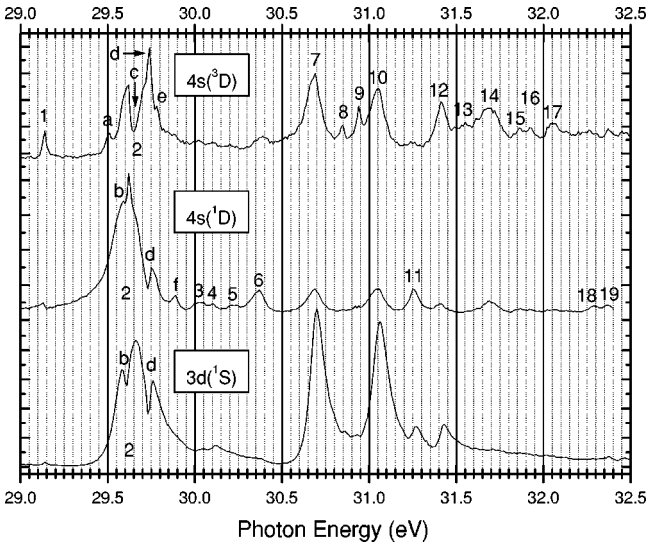

FIG. 4. CIS scans of the main lines focusing on photon-energy region I. Vertical lines for each tick mark are shown so that the photon energy can be easily traced from the top to the bottom of the figure.

marked *b* and *d*. This type of behavior has been seen before in the case of Mn [3,16] where there is a dip in the main $3p \rightarrow 3d$ giant resonance and also in Cd [23]. Similar behavior has been predicted in the $4s$ cross section of Mn^+ in the region of the $3p \rightarrow 3d$ giant resonance [24]. In Ref. [16] this dip was ascribed to another resonance that sits virtually atop of the giant resonance and strongly interacts with it, effectively ''stealing'' intensity from it. We propose that the same mechanism is at work here. This interpretation also explains the appearance of feature 2 in the $4s(^1D)$ channel. In this channel, resonance 2 is much less asymmetric than in the $3d(^1S)$ channel. Nevertheless, as can be seen from Fig. 4 the dips in feature 2 very nearly coincide with *b* and *d* in the $3d(^1S)$ channel and have, therefore, been given the same designation, although *b* in this channel is much less window-like than in the $3d(^1S)$ channel.

TABLE III. Approximate Sc I resonance energies in eV, between 29.0 and 32.5 eV.

Line	This work	Ref. [10]	Line	This work	Ref. [10]
1	29.13(1)		8	30.83(1)	
a	29.50(1)		9	30.92(1)	
b	29.60(1)		10	31.03(1)	31.06(6)
2	29.62(1)	29.61(7)	11	31.24(1)	31.25(7)
c	29.64(1)		12	31.39(1)	31.45(7)
d	29.72(1)	29.74(6)	13	31.51(3)	
e	29.76(1)		14	31.68(1)	
f	29.88(1)		15	31.84(1)	
3	30.01(1)		16	31.91(1)	
4	30.09(1)	30.07(10)	17	32.04(1)	
5	30.21(1)		18	32.27(1)	
6	30.36(1)		19	32.35(1)	
7	30.68(1)	30.67(6)			

This simple interpretation, however, appears to fail for the $4s(^3D)$ channel. Interestingly and somewhat surprisingly, resonance 2 appears dramatically different in the two $4s$ channels, which differ only in their spin multiplicities. In the case of Mn [16], for example, there are relatively minor differences in the cross sections of the $4s(^7S)$ and the $4s(^5S)$ lines in the region of the $3p\rightarrow 3d$ giant resonance. The position of feature *c* has been placed in the large ''valley,'' which has a minimum at 29.65 eV in Fig. 4. There appears to be no counterpart to this feature in either of the other two channels. This also appears to be the case for features *a* and *e*. One could argue that *e* is simply due to statistical variations. However, this feature is reproducible as it was observed in another CIS spectrum of somewhat lower quality. It could be, however, that *e* is a manifestation of the interaction of *d* with resonance 2 and only appears to be a separate resonance. Note that in this channel *d* is not windowlike as in the $4s(^1D)$ and $3d(^1S)$ channels. One possible explanation for the apparent difference of resonance 2 in the $4s(^3D)$ channel is that a different set of overlapping resonances are interacting with it as compared to the other two main line channels. This, however, is merely speculation. A definitive explanation of the intriguing shape of resonance 2 in these three channels will have to await a detailed theoretical analysis.

As noted above, region I of the CIS scans contains the narrowest features, e.g., *b* in the $4s(^1D)$ channel, *d* in the $4s(^3D)$ channel, and resonances 1, 8, and 9. A separate CIS scan at a higher resolution, $E/\Delta E\approx 5200$ and 2-meV steps, over peaks 8 and 9 showed no significant change in the width of the lines. From this we conclude that the observed widths of all resonances in all CIS spectra are dominated by their natural widths. The nominal FWHM of features 1, 8, and 9 is about 20 meV. Other features, e.g., 7 and 10, are considerably wider, about 110 meV.

2. Satellite lines

CIS scans were recorded on all major satellites indicated by the asterisks in Fig. 1. The spectrometer resolution used for these measurements corresponds to a FWHM of 280 meV. Because this spectrometer resolution was roughly a factor of 2 lower than what was obtained in the lower panel of Fig. 1, no CIS scans were carried out for satellites 5 and 7 because of their proximity to stronger neighboring lines. Furthermore, no recordings were made on the weakest satellites, i.e., 9, 12, and 14. A quantitative estimation of the degree of overlap between closely spaced satellite lines was determined by fitting PES spectra of the satellites recorded at $h\nu=36.0$ or 35.9 eV. The following results were obtained: sat. 3, a 4% contribution from the $4s(^1D)$ mainline; sat. 6, an 8% contribution from sat. 7; sat. 8, less than a 2% contribution from sat. 7 and less than 3% from sat. 9; sat. 11, less than a 3% contribution from sat. 12; sat. 13, less than a 9% contribution from the sat. 12 and a negligible contribution from sat. 14; sat. 15, a negligible contribution from sat. 14 and sat. 16; and sat. 16, less than an 11% contribution from sat. 15. Hence, nearly all CIS satellite spectra can be regarded as being very pure throughout.

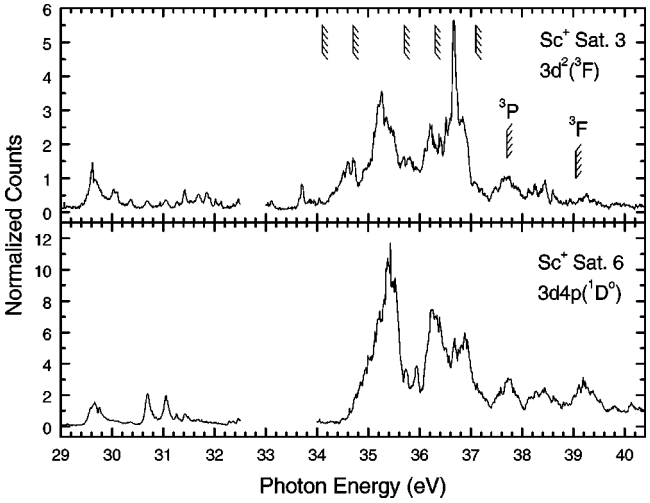

FIG. 5. CIS scans of satellites 3 and 6 recorded at the magic angle covering the region of the $3p\rightarrow nl$ resonances including the $3p\rightarrow 3d$ giant resonance. Otherwise as for Fig. 2.

Due to time constraints, only satellites 3 and 6 had CIS scans recorded in region I. Their spectra are displayed in Fig. 5. In region I, sat. 3 more closely resembles the two $4s$ main lines than the $3d$ main line. In photon-energy region II, there is a very close resemblance to the $4s(^3D)$ main line, in particular for the group of resonances centered around $h\nu=35.24$ and 36.6 eV. For sat. 6, region I appears very similar to what is observed for the $3d(^1S)$ main line. In region II, however, it does not really mimic any of the main lines, although it shares characteristics that can be found in all the main line channels. Otherwise, the behavior of region I with respect to region II for each satellite is generally the same as for the main line channels. That is, the resonances in region I are generally more separated and narrower than those found in region II.

Figure 6 shows the CIS scans of satellites 8, 10, and 11 and Fig. 7 shows them for satellites 13, 15, and 16. For the most part, all spectra look rather different. About the only common characteristic between all of them is the group of resonances that appear around $h\nu=35.24$ and 36.60 eV. These are the same resonances that appear with the greatest intensity in the main lines, see Fig. 2. However, the intensity distributions of these resonances in each satellite and main line are in general quite different from each other. This is even true for those satellites that have the same principle configuration, for example, satellites 6 and 8, which are both $3d4p$; satellites 10 and 11, which are $4s4p$; and satellites 13, 15, and 16, which are $3d4d$. This is a strong indication of the importance of the *LS* term in determining the decay dynamics associated with the production of each satellite. In addition, the structure of sats. 8 and 10 in the region around $h\nu=35.24$ eV clearly indicates that there are more than two resonances present. Hence, the broad feature seen at this photon energy in the main lines is clearly a composite of several resonances as asserted earlier.

In contrast to the other CIS spectra, those displayed in Fig. 7, sats. 13, 15, and 16, all have substantial intensity in the region between roughly $h\nu=35.6$ and 36.4 eV where the

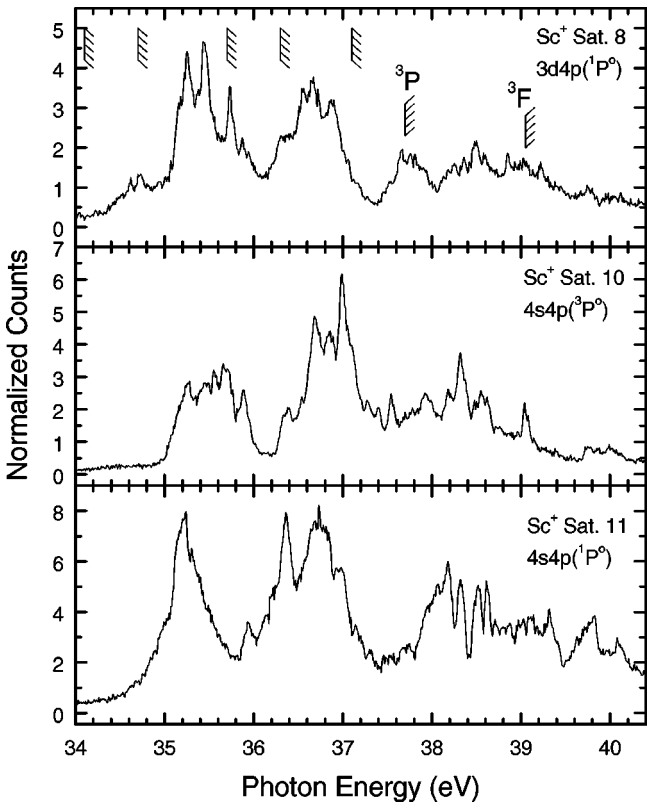

FIG. 6. CIS scans of satellites 8, 10, and 11 recorded at the magic angle in the photon-energy region of the higher resonances (region II). Otherwise as for Fig. 2.

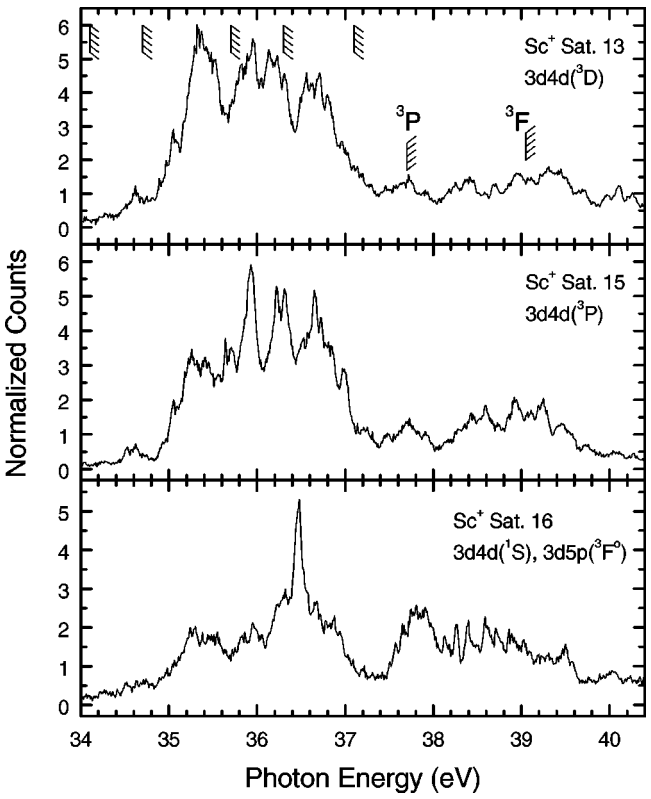

FIG. 7. CIS scans of satellites 13, 15, and 16 recorded at the magic angle in the photon-energy region of the higher resonances (region II). Otherwise as for Fig. 2.

other satellites and main lines have a valley. These satellites all have even parity with configurations of the form $3d4d$, although sat. 16 is probably a composite feature that includes a mixture of the $3d5p$ configuration, see Table I. The enhancement of the resonances in this region in these particular channels may provide a hint as to their identification.

3. CIS sum

The sum of all CIS spectra is presented in Fig. 8. Such a spectrum is equivalent to the total cross section for photoionization *if* all channels, including multiple photoionization, are included and fluorescence decay of the excited states is negligible compared to autoionization. For the spectra recorded in this work, most but not all of the satellite channels are accounted for and we expect fluorescence to be negligible. With regards to multiple ionization processes, our experimental methods did not allow us to make any definitive estimate of their potential contribution. In addition to some of the satellite channels that are missing, contributions from direct $3p$ photoionization are also absent. This includes $3p$ photoionization from the $[\mathrm{Ar}]3d^2(^1D)4s(^2S)$ part of the ISCI ground state as well as from the primary $[\mathrm{Ar}]3d(^2D)4s^2(^1S)$ part of the ISCI ground state, see Eq. (3.1). The former becomes possible at photon energies above $h\nu = 34.1$ eV and the latter above $h\nu = 37.7$ eV. It is not clear how strong the low-lying $3p$ ionization channels are, as they were not investigated in this work. Inclusion of all of these ionization channels would lead to a steplike increase in the total cross section at each respective threshold. The energies of additional $3p$ ionization thresholds associated with the other two parts of the ISCI ground state are likely to lie outside the photon-energy region investigated here, although we have no way of confirming this. Hence, one can expect that this CIS sum spectrum will start to deviate from the photoabsorption data of atomic Sc at photon energies above 34.1 eV. This is borne out in a comparison of our CIS sum

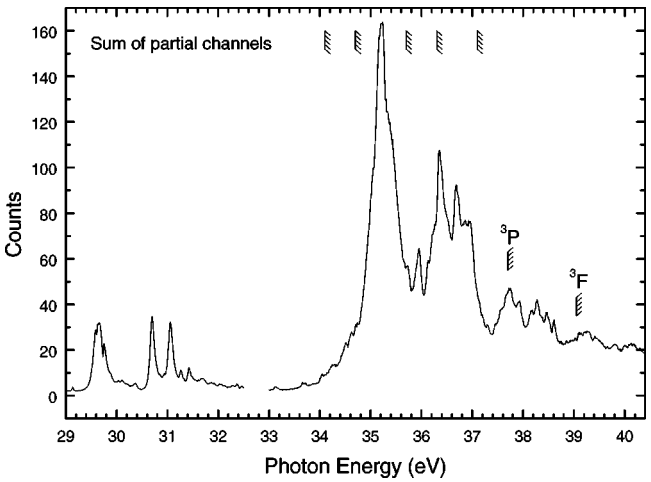

FIG. 8. Sum of all measured partial cross sections as shown in Figs. 3, 5–7. Region I is nearly equivalent to an absorption spectrum, whereas region II will be similar but not equivalent.

spectrum with the photoabsorption data of Ref. [3]. These differences aside, there is generally good agreement between our results and the lower-resolution absorption data with one additional exception. As noted in earlier studies [3,10], the absorption data reveal a broad and prominent peak at $h\nu \simeq 40$ eV, which does not appear in any of our partial cross sections nor in those of Ref. [10]. The origin of this feature is not entirely clear, but is attributed to a $3p \rightarrow \varepsilon d$ continuum resonance [3].

C. Comparison with theory

Calculations of the partial cross sections of the Sc $4s$ and $3d$ main lines in the region of the $3p \rightarrow 3d$ giant resonance have been recently made using many-body perturbation theory (MBPT) [9]. Only final states resulting from $3p$, $3d$, and $4s$ photoionization of the primary configuration of Eq. (3.1) in *LS* coupling were considered. As noted earlier, even in this approximation, this yields nine different ionic states and 32 different channels. Ground-state correlation was included by using first-order perturbation theory to correct the ground-state wave function (generated in the Hartree-Fock approximation). This was done by including additional states that involved one- and two-particle excitations from the Hartree-Fock ground state that also had nonzero, dipole matrix elements with one of the aforementioned final states. These ground-state correlations were then applied to correct the dipole matrix elements to lowest order. All significant first-order corrections were included in the calculations. Interestingly, mixings of the type $3p^6 3d4skd$ and $3p^5 3d4skd$ $(k=n,\varepsilon)$ were not included because their effects were found to be very small. The final states in the calculation were not corrected for electron correlation by mixing with additional configurations, rather those having the same final *LS* term were diagonalized. This is basically an intermediate coupling approach applied to *LS*-specified wave functions. Finally, no excitation with ionization was considered, i.e., satellite channels were completely neglected in the calculation. For further details see Ref. [9].

A comparison of our experimental data with the theoretical partial cross sections of Ref. [9] after convolution with a bandpass of 20 meV is shown in Fig. 9. The theoretical spectra were normalized as follows. The maximum of the theoretical $3d(^1S)$ cross section at $h\nu = 29.8$ eV, the $[3p^5(3d^2\ ^1G)4s^2](^2F)$ resonance according to theory, was arbitrarily set to be the same as the experimental $3d(^1S)$ cross section maximum at $h\nu = 29.65$ eV. The same scaling factor was then applied to the other partial cross sections. While this is not the only possible scheme by which theory can be normalized to experiment, it is probably the most reasonable. Two other alternatives are (i) normalizing the integrated intensity of the theoretical $[3p^5(3d^2\ ^1G)4s^2](^2F)$ resonance in the $3d$ channel to match the experimental value between $h\nu = 29.4$ and 30.4 eV, and (ii) scaling the theoretical spectrum in the $3d$ channel such that its *total* integrated intensity matches the *total* experimental integrated intensity. In the former case this would reduce the overall theoretical intensity compared to experiment in the $3d$ channel, and in the latter case it would greatly magnify the theoretical intensity. With regard to the theoretical photon-energy scale, no shift has been made.

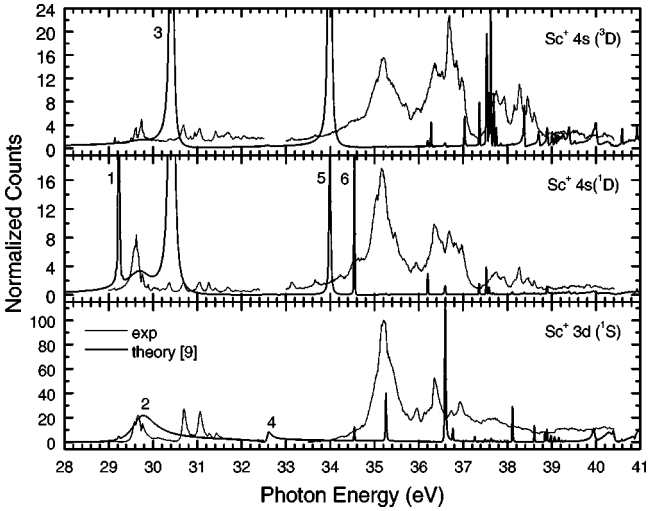

FIG. 9. A comparison of the experimental and theoretical partial cross sections for the $4s$ and $3d$ main lines in the region of the $3p \rightarrow nl$ excitations. The numbers correspond to the first six resonances of the $3p \rightarrow 3d$ excitations as predicted by theory.

It is immediately apparent from Fig. 9 that there is little agreement between theory and experiment. As the resolution of the experimental spectra is lifetime limited, one cannot attribute discrepancies between experiment and theory to result from insufficient experimental resolution. The primary discrepancies between theory and experiment can be summarized as follows.

(i) The greatest intensity in all channels except for the $4s(^3D)$ are predicted to be in region I, where experiment finds the weakest intensity. Of the nine possible excited states arising from $3p \rightarrow 3d$ excitation in *LS* coupling, theory predicts the first four to occur in region I. These resonances and the next two are indicated with numbers in Fig. 9. The remaining three, which occur at photon energies of 39.54, 39.95 and 40.00 eV have very small cross sections and are not indicated in Fig. 9. According to Ref. [9] the labeled resonances have the following designations:

feature 1 $[\mathrm{Ne}]3s^2 3p^5(3d^2\ ^1D)4s^2(^2P)$

feature 2 $[\mathrm{Ne}]3s^2 3p^5(3d^2\ ^1G)4s^2(^2F)$

feature 3 $[\mathrm{Ne}]3s^2 3p^5(3d^2\ ^1D)4s^2(^2D)$

feature 4 $[\mathrm{Ne}]3s^2 3p^5(3d^2\ ^1D)4s^2(^2F)$

feature 5 $[\mathrm{Ne}]3s^2 3p^5(3d^2\ ^3P)4s^2(^2D)$

feature 6 $[\mathrm{Ne}]3s^2 3p^5(3d^2\ ^1S)4s^2(^2P)$.

These states are not pure, but are mixtures of states that have the same final *LS* term. The designations given above correspond to the $3d^2$ term in the eigenvector with the greatest weight.

(ii) In region II, where experiment finds the strongest and broadest transitions to be present, theory mostly predicts rather weak and very narrow transitions.

(iii) In region II where experiment finds numerous overlapping and likely interacting resonances, theory predicts generally very sparse spectra. Furthermore, there seems to be almost no correlation between the predicted positions of the resonances in this region and the observed positions.

(iv) Relative to the $3d(^1S)$ partial cross section, theory predicts much larger partial cross sections for the two $4s$ main lines than is observed, especially in region I.

Clearly, an important aspect of the photoionization process has not been included in these calculations. What follows are some possible explanations as to why theory agrees so poorly with experiment.

(1) *LS* coupling is not adequate, even though this is a low-*Z* element. This will be most important for the intermediate excited states, where additional excitation channels will become possible. Although not likely to be the decisive factor in removing the discrepancy between experiment and theory by going beyond *LS* coupling excitation from the excited $^2D_{5/2}$ state, which lies only 20 meV above the the $^2D_{3/2}$ ground state, can be included. Recall, that due to the operating temperature of the oven, 56% of the target atoms are in this state as opposed to the ground state. The Hartree-Fock calculations of Ref. [10], which were published in part in Ref. [3], included this excited state explicitly. Specifically, energies and oscillator strengths were determined from the following types of transitions:

$$\begin{aligned}[\mathrm{Ne}]3s^2 3p^6 3d 4s^2(^2D_{3/2,5/2}) \\ \rightarrow a(\%)[\mathrm{Ne}]3s^2 3p^5 3d^2(^1X)4s^2(^2L_{j,j'}) \\ + b(\%)[\mathrm{Ne}]3s^2 3p^5 3d^2(^3Y)4s^2(^2L_{j,j'}),\end{aligned} \tag{3.4}$$

where the final terms can be $^2P_{1/2,3/2}$, $^2D_{3/2,5/2}$, or $^2F_{5/2,7/2}$. The results of these calculations indicate that the transitions with the largest oscillator strengths do in fact occur in region II. For example, the feature at $h\nu = 35.24$ eV is ascribed to be primarily two resonances which, in accordance with Eq. (3.4), are designated 46% $(^1G)^2F_{5/2} + 54\%$ $(^3F)^2F_{5/2}$ and 48% $(^1G)^2F_{7/2} + 52\%$ $(^3F)^2F_{7/2}$. According to the calculation, they are split by 160 meV. In contrast, the MBPT calculation of Ref. [9] assigns this feature to a $[\mathrm{Ne}]3s^2 3p^5 3d 4s^2(^3P)5s(^2P)$ excited state resulting from a $3p \rightarrow 5s$ transition. As this is generally the strongest feature observed in all channels, it is difficult to believe that it is not associated with a $3p \rightarrow 3d$ transition. Both calculations essentially agree on the designation of the resonance associated with the features having a photon energy of about 29.6 eV, i.e., feature 2 in the MBPT calculation. In the calculation of Ref. [10] these features are assigned to the 51% $(^1G)^2F_{5/2} + 42\%$ $(^3F)^2F_{5/2}$ and 48% $(^1G)^2F_{7/2} + 43\%$ $(^3F)^2F_{7/2}$ excited states. For both calculations, the degree of mixing of configurations with different $3d^2$ terms is quite comparable. While it would seem that the Hartree-Fock calculation of Ref. [10] gives a better qualitative agreement with experiment, it too has shortcomings, specifically with regard to which transitions have the greatest oscillator strength. Of the three strongest resonance groups seen in absorption and in our CIS-sum spectrum, Fig. 8, the most intense are those located around $h\nu = 35.2$ eV, followed by those around $h\nu = 36.5$ eV with the weakest around $h\nu = 38$ eV. According to theory, the most intense resonances occur around $h\nu = 38$ eV $(gf = 21.3)$, followed by those around $h\nu = 35.2$ eV $(gf = 16.8)$, with the weakest of these three groups around $h\nu = 36.5$ eV $(gf = 10.4)$. In addition, only two resonances are predicted to fall into each group, where as argued above, there are certainly more than two resonances that makeup each of these resonance groups.

(2) The satellite channels *cannot* be ignored. As described in Sec. III A, the appearance of valence satellites off resonance is most likely due to ISCI. This has two important consequences. The first is that it greatly expands the possible number of excited states that can arise from $3p$ excitation, see Eq. (3.3). As noted above, the MBPT calculation predicts very sparse spectra in region II, while experimentally the CIS spectra are very resonance rich in this region. Clearly some mechanism is necessary to ''generate'' the additional resonances that are seen experimentally. Secondly, the presence of the satellites in the final state opens up additional decay pathways. The presence of these additional pathways will cause a redistribution of the decay strength in the main lines, as some excited states may now preferentially decay into the satellite channels rather than the main line channels. While the decay to individual satellites may be weak in comparison to the main lines, as seen in the data, when viewed collectively the transitions are not negligible. Recall that at the maximum of the $3p \rightarrow 3d$ transition at $h\nu = 35.24$ eV, nearly 28% of all the observed intensity is in the satellites. Hence, the presence of the satellites could significantly alter the decay dynamics of the main lines. Furthermore, the presence of satellite channels will have the salutary effect of broadening the resonances as observed experimentally. This will be especially important for the higher-lying Rydberg states as they will preferentially autoionize into the satellite channels (spectator Auger decay). Inclusion of such decay channels has been shown to have a significant impact on the width of the intermediate states in the case of $2p$ excitation and decay in Ar [25]. As noted earlier, the MBPT calculation did not take into account satellite processes. Of course, the validation of these conjectures will have to await a calculation above and beyond what was done using the MBPT method of Ref. [9] or the Hartree-Fock approach of Ref. [10].

IV. CONCLUSIONS

We have carried out a high-resolution study of atomic Sc covering the $3p \rightarrow nd$, ms resonance region with a specific emphasis on the relative partial cross sections of all main lines and the majority of the associated satellite lines. In contrast to an earlier experimental study [3,10], we have completely separated the cross section of the $4s(^1D)$ from that of the $4s(^3D)$, indicating rather different behavior for each. The superior resolution in this case has revealed additional structure in all channels as well as distinct differences

in the spectral appearance of these channels that was not seen in the earlier work. Due to the very complicated and rich structure of the spectra, no attempt has been made to assign resonance energies or to classify the observed resonances [26]. Aside from the overlap of numerous resonances, there is likely to be interactions amongst them as well. There is clear evidence for this in the peculiar shape of the feature that appears at about $h\nu = 29.6$ eV in the CIS scans of all the main lines. All observed widths are seen to be lifetime limited and the deduced natural widths are found to vary significantly.

We also carried out a detailed determination of the fine-structure properties of the $3p$ lines at $h\nu = 90$ eV. Our results of the binding energies and relative intensities are in very good agreement with a recent experiment [19,20]. Theoretical binding energies [9] are in reasonable agreement with experiment except for the $3p(^1P)$ term. There is, however, some uncertainty regarding the peak assignments with regard to the ^1D, ^3D, and ^1F terms.

A comparison of our CIS data with the most recent and extensive calculation reveals major discrepancies. Theory predicts the strongest resonances to occur in that part of the experimental spectrum where the resonances are clearly the weakest. Where experiment finds numerous overlapping and strong resonances, theory predicts rather sparse spectra generally composed of very weak resonances. The origins of these discrepancies are not known, but could arise from the use of LS coupling in the calculation and lack of inclusion of satellite processes that are clearly observed with significant intensity both on and off resonance.

With the present data as a guide, it should be possible to develop a theoretical model that might explain the gross features of the electronic structure and dynamics of scandium, the ''simplest'' open-shell atom with a partially filled *d* subshell.

ACKNOWLEDGMENTS

The authors would like to thank Dr. Zikri Altun and Dr. Steve Manson for making the numerical results of their calculations available to us. This work was supported in part by an internal research grant from the University of Wisconsin–Eau Claire. M.O.K. acknowledges support from NSF Grant No. PHY-9507573. The University of Wisconsin SRC is operated under the National Science Foundation Grant No. DMR-9531009. Support by the staff at SRC is gratefully acknowledged.

[1] V. Schmidt, Rep. Prog. Phys. **55**, 1483 (1992), and references therein.
[2] G. B. Armen, H. Aksela, T. Åberg, and S. Aksela, J. Phys. B **33**, R49 (2000), and references therein.
[3] B. Sonntag and P. Zimmermann, Rep. Prog. Phys. **55**, 911 (1992), and references therein.
[4] M. O. Krause, Nucl. Instrum. Methods Phys. Res. B **87**, 178 (1994), and references therein.
[5] A. F. Starace, R. H. Rast, and S. T. Manson, Phys. Rev. Lett. **38**, 1522 (1977).
[6] S. T. Manson and A. F. Starace, Rev. Mod. Phys. **54**, 389 (1982).
[7] S. B. Whitfield, K. Kehoe, M. O. Krause, and C. D. Caldwell, Phys. Rev. Lett. **84**, 4818 (2000).
[8] F. Robicheaux and C. H. Greene, Phys. Rev. A **48**, 4429 (1993); **48**, 4441 (1993).
[9] Z. Altun and S. T. Manson, Europhys. Lett. **33**, 17 (1996); Phys. Rev. A **59**, 3576 (1999).
[10] H. E. Wetzel, dissertation, University of Hamburg, 1987 (unpublished).
[11] R. Reininger, S. L. Crossley, M. A. Lagergren, M. C. Severson, and R. W. C. Hansen, Nucl. Instrum. Methods Phys. Res. A **347**, 304 (1994).
[12] R. E. Honig and D. A. Kramer, *Vapor Pressure Data for the Solid and Liquid Elements*, RCA Rev. **30**, 2 (1969).
[13] J. Sugar and C. Corliss, J. Phys. Chem. Ref. Data Suppl. **14**, 2 (1985).
[14] K. Codling, R. P. Madden, and D. L. Ederer, Phys. Rev. **155**, 26 (1967).
[15] R. P. Madden, D. L. Ederer, and K. Codling, Phys. Rev. **177**, 136 (1969).
[16] S. B. Whitfield, M. O. Krause, P. van der Meulen, and C. D. Caldwell, Phys. Rev. A **50**, 1269 (1994).
[17] J. M. Dyke, B. W. J. Gravenor, M. P. Hastings, G. D. Josland, and A. Morris, J. Electron Spectrosc. Relat. Phenom. **35**, 65 (1985).
[18] U. Becker and D. A. Shirley, Phys. Scr. **31**, 56 (1990), and references therein.
[19] K. Tiedtke, Ch. Gerth, M. Martins, B. Obst, and P. Zimmermann, J. Phys. B **33**, L755 (2000).
[20] K. Tiedtke and P. Zimmermann (private communication).
[21] M. O. Krause, R. Wehlitz, S. B. Whitfield, and C. D. Caldwell (unpublished).
[22] M. Meyer, Th. Prescher, E. von Raven, M. Richter, E. Schmidt, B. Sonntag, and H.-E. Wetzel, Z. Phys. D: At., Mol. Clusters **2**, 347 (1986).
[23] J. Jimenez-Mier, C. D. Caldwell, and M. O. Krause, Phys. Rev. A **39**, 95 (1989).
[24] V. K. Dolmatov, J. Phys. B **25**, L629 (1992).
[25] T. W. Gorczyca and F. Robicheaux, Phys. Rev. A **60**, 1216 (1999).
[26] We have compiled a listing of the discernible resonance positions for comparison with any future experiment or theoretical result. The results can be obtained upon request.